




Article

TiO₂ Nanobelt@Co₉S₈ Composites as Promising Anode Materials for Lithium and Sodium Ion Batteries

Yanli Zhou ¹, Qian Zhu ², Jian Tian ^{3,*}  and Fuyi Jiang ^{1,*}

¹ School of Environmental and Material Engineering, Yantai University, Yantai 264005, China; zhouyanli@ytu.edu.cn

² Key Laboratory of Colloid and Interface Chemistry, Ministry of Education School of Chemistry and Chemical Engineering, Shandong University, Jinan 250100, China; 879391733@163.com

³ School of Materials Science and Engineering, Shandong University of Science and Technology, Qingdao 266590, China

* Correspondence: jiantian@sdust.edu.cn (J.T.); fyjiang@ytu.edu.cn (F.J.); Tel.: +86-0532-86057929 (J.T.); +86-0535-6706039 (F.J.); Fax: +86-0532-86057929 (J.T.); +86-0535-6706038 (F.J.)

Received: 9 August 2017; Accepted: 28 August 2017; Published: 2 September 2017

Abstract: TiO₂ anodes have attracted great attention due to their good cycling stability for lithium ion batteries and sodium ion batteries (LIBs and SIBs). Unfortunately, the low specific capacity and poor conductivity limit their practical application. The mixed phase TiO₂ nanobelt (anatase and TiO₂-B) based Co₉S₈ composites have been synthesized via the solvothermal reaction and subsequent calcination. During the formation process of hierarchical composites, glucose between TiO₂ nanobelts and Co₉S₈ serves as a linker to increase the nucleation and growth of sulfides on the surface of TiO₂ nanobelts. As anode materials for LIBs and SIBs, the composites combine the advantages of TiO₂ nanobelts with those of Co₉S₈ nanomaterials. The reversible specific capacity of TiO₂ nanobelt@Co₉S₈ composites is up to 889 and 387 mAh·g⁻¹ at 0.1 A·g⁻¹ after 100 cycles, respectively. The cooperation of excellent cycling stability of TiO₂ nanobelts and high capacities of Co₉S₈ nanoparticles leads to the good electrochemical performances of TiO₂ nanobelt@Co₉S₈ composites.

Keywords: TiO₂ nanobelt@Co₉S₈; mixed phases; cycling stability; lithium ion batteries (LIBs); sodium ion batteries (SIBs)

1. Introduction

Lithium-ion batteries (LIBs), as one of the most important energy storage devices, have attracted extensive attention due to their advantages of high energy density and long cycle life [1,2]. However, the practical application of LIBs is still restricted especially in electrical devices and hybrid electric vehicles (HEV). Electrodes materials are key factors to affect the electrochemical performance for energy storages devices [3]. The commercial graphite anode for LIBs cannot meet the ever-increasing requirement owing to its low specific capacity (372 mAh·g⁻¹) and the safety problems [4]. Therefore, more attention has been focused on designing new anode materials to replace graphite [5–10]. Among various transition metal oxides, Titanium dioxide (TiO₂) has been considered as new anode materials for both LIBs and SIBs because of its low cost, environmental friendliness, high voltage platform, and long cycling stability [11–15].

One-dimensional (1D) TiO₂ nanomaterials such as nanowires, nanotubes, and nanorods have been investigated as anodes, which effectively improved the ionic and electronic transport properties compared to TiO₂ nanoparticles [16–19]. TiO₂ nanobelt is one of the potential candidates among these materials in energy storage fields [20,21]. However, the intrinsic low theoretical capacity of TiO₂ still

limits its wide application. Thus, many effective methods have been adopted to increase its inherent low specific capacity. An efficient way is to hybridize TiO_2 with another active material with high capacity. The composites synthesized by TiO_2 and metal oxides or sulfides delivered excellent lithium storage performances [22–24]. For instance, the 3D electrode by assembling Fe_2O_3 hollow nanorods onto highly oriented TiO_2 nanotube arrays delivered a high capacity of over $600 \text{ mAh}\cdot\text{cm}^{-2}$ at a current density of $100 \text{ mA}\cdot\text{cm}^{-2}$ after 50 cycles [23]. Furthermore, the $\text{TiO}_2@ \text{MoS}_2$ hybrid exhibited a reversible capacity of $710 \text{ mAh}\cdot\text{g}^{-1}$ after 100 cycles at $100 \text{ mA}\cdot\text{g}^{-1}$ [24]. Another common method is to change the crystal phases of TiO_2 to enhance its electrochemical performance. Very recently, TiO_2 -B anode materials have attracted great interest for both LIBs and SIBs [25–28]. They presented better electrochemical performances than the other phases of TiO_2 due to their open tunnel structure and pseudocapacitive lithium storage properties [29,30]. Besides, it has been reported that the anatase/ TiO_2 -B coherent interfaces could contribute to additional lithium storage, leading to better electrochemical performances than single phase TiO_2 [31]. TiO_2 -B related composites have also become the research focus for LIBs. For example, the hierarchical TiO_2 -B nanowire@ α - Fe_2O_3 composites exhibited better cycling stability than pure TiO_2 -B [32]. In addition, the TiO_2 -B nanoribbons anchored with NiO nanosheets as anode materials also displayed good cycling stability at a large rate of 5 C [33]. Cobalt sulfides as high capacity anodes have so many distinct advantages, such as the good conductivity, low electrode polarization and good thermal stability compared with transition metal oxides. However, to our knowledge, the composites of anatase/ TiO_2 -B nanobelt and cobalt sulfides have not been reported yet for both LIBs and SIBs.

In this paper, TiO_2 nanobelt@ Co_9S_8 composites have been successfully obtained via a solvothermal reaction and high-temperature calcination process. The composites as anode materials for both LIBs and SIBs present good electrochemical performances, which is better than single TiO_2 nanobelts and Co_9S_8 nanoparticles. The high reversible capacity, good cycling stability and rate capability of TiO_2 nanobelt@ Co_9S_8 composites are likely attributed to the synergistic effect of Co_9S_8 nanoparticles and anatase/ TiO_2 -B nanobelts.

2. Materials and Methods

2.1. Synthesis of mixed Phase TiO_2 Nanobelt@ Co_9S_8 Composites

Mixed phase TiO_2 nanobelts were prepared by a previously reported method [34]. TiO_2 nanobelt@ Co_9S_8 composites were synthesized via the following preparation procedure: First, 30 mg TiO_2 nanobelts glucose aqueous solution (25 mL, 0.05 M) was dispersed by ultrasonic treatment for 2 min. Then 1.5 mmol of cobalt acetate were added into this solution and stirred for another 20 min to form a homogeneous dispersion. After that, 4.5 mmol of thiourea in ethylene glycol (25 mL) was added into the above mixture. The obtained dispersion was transferred to a Teflon-lined stainless steel autoclave and then heated at $180 \text{ }^\circ\text{C}$ for 10 h. After it was cooled to room temperature, the precipitate was collected, washed with deionized water and absolute alcohol thoroughly, and dried at $60 \text{ }^\circ\text{C}$ for 12 h. Finally, the TiO_2 nanobelt@ Co_9S_8 composites were obtained through annealing the precipitate at $650 \text{ }^\circ\text{C}$ for 10 h under Ar/H_2 (5%) atmosphere. Co_9S_8 nanoparticles were also prepared according to the methods reported in previous paper [35].

2.2. Sample Characterization

X-ray diffraction (XRD) patterns were carried out by a Bruker D8 advanced X-ray diffractometer using monochromatic $\text{Cu K}\alpha$ radiation ($\lambda = 1.5418 \text{ \AA}$). Transmission electron microscope (TEM) images and high-resolution transmission electron microscopy (HRTEM) images were achieved on a high-resolution transmission electron microscope (JEOL-2100, Akishima, Tokyo, Japan). Scanning electron microscope (SEM) images, mapping images, and energy dispersive spectrometer (EDS) spectrum were taken from a field-emission scanning electron microscope (FEI Nova 450, Hillsboro, OR, USA). Raman spectra were obtained on a MicroRaman spectrometer using a laser of 532 nm as

an excitation (LabRAM HR Evolution, Kyoto, Japan). Nitrogen sorption isotherm was examined on a Micromeritics ASAP2020HD88 gas sorptometer at 77.3 K (Micromeritics, Norcross, GA, USA).

2.3. Electrochemical Measurements

Electrochemical performances of various electrodes were evaluated by CR2032 coin cells. The working electrode was fabricated by coating a mixture of 70 wt % of active material, 20 wt % of acetylene black, and 10 wt % of binder CMC (carboxyl methyl cellulose) in deionized water on a clean copper foil. Then the obtained foil was dried in vacuum at 60 °C for 10 h. The resulting foil was roll-pressed and punched into discs with a diameter of 12 mm. The mass loading of active material is estimated to 1.0–1.5 mg·cm⁻². The coin cells were assembled in an Ar-filled glovebox. For LIBs, the lithium foil was used as the counter electrode, Celgard 2400 microporous polypropylene membrane as the separator, and a solution of 1 M LiPF₆ in ethylene carbonate (EC) and dimethyl carbonate (DMC) (1:1 *v/v*) as the organic electrolyte. For SIBs, the sodium foil was used as the counter electrode, glass fiber was used as the separator, and the electrolyte is a solution of 1 M NaClO₄ in EC and diethyl carbonate (DEC) (1:1 *v/v*) containing of 2 wt % fluoroethylene carbonate (FEC). Galvanostatic charge-discharge curves were acquired in a range of 0.01 to 3 V on the battery cyclers (Land CT2001A, Wuhan, China). Electrochemical impedance spectra (EIS) were carried out on an electrochemical workstation (AUTOLAB PGSTAT302N, Herisau, Switzerland) over a frequency range of 100 kHz to 0.01 Hz. Cyclic voltammetry (CV) curves were measured on an electrochemical workstation (CHI660E, Shanghai, China) over 0.01 to 3 V at a scanning rate of 0.1 mV·s⁻¹. All the electrochemical tests were performed at 25 °C.

3. Results and Discussion

Figure 1 shows the preparation process of TiO₂ nanobelt@Co₉S₈ composites. Firstly, the mixed phase TiO₂ nanobelts were prepared via a three step chemical reaction and annealing [34]. Secondly, the intermediate products labeled as TiO₂ nanobelt@a-Co_xS_y were obtained by a solvothermal reaction, using mixed phase TiO₂ nanobelts as growth templates and glucose as a linker. Finally, TiO₂ nanobelt@Co₉S₈ composites were formed with the initial amorphous Co_xS_y changing into crystalline Co₉S₈ after an annealing treatment of 650 °C for 10 h under Ar/H₂ atmosphere.

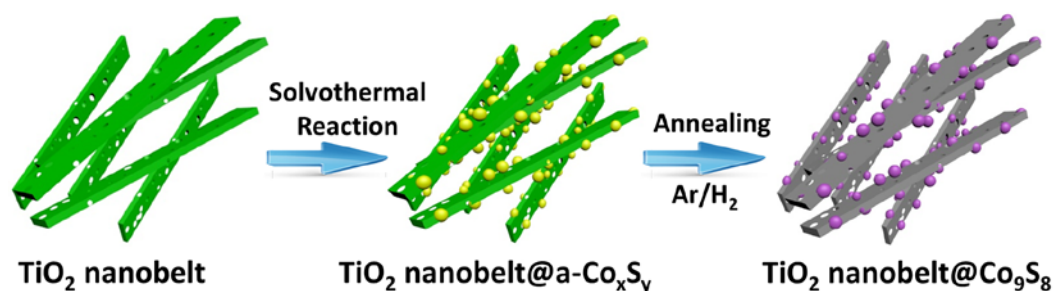


Figure 1. Preparation process of TiO₂ nanobelt@Co₉S₈ composites.

3.1. Characterization of Samples

Figure 2 shows the XRD pattern of obtained TiO₂ nanobelt@Co₉S₈ composites. Three diffraction peaks marked with blue rhombus can be assigned to (311), (222) and (440) planes of cubic-phase Co₉S₈ (JCPDS Card, No. 65-1765) [8]. The diffraction peaks located at 2θ~25.3°, 48.0°, 53.9°, 55.1° and 62.7° can be identified as anatase TiO₂ (JCPDS Card, No. 21-1272) [13]. The weak diffraction peak at 44.5° is attributed to TiO₂-B (JCPDS Card, No. 46-1237) [16]. Meanwhile, mixed phase TiO₂ nanobelt has been clearly demonstrated by the XRD patterns (Figure S1a and b). The Raman spectra of as-obtained TiO₂ nanobelt and annealed treated TiO₂ nanobelt also verify above results. As shown in Figure S1c and Figure S1d, two strong peaks located at 145 and 640 cm⁻¹ are attributed to both anatase and

TiO₂-B, and one weak peak at 517 cm⁻¹ is ascribed to anatase TiO₂. All the remaining peaks are originated from TiO₂-B [36]. EDS spectrum was measured to further verify the element composition and contents of the composites (Figure S2). The TiO₂ contents (wt %) in the composites is estimated as ~64%, in which C and Al is from the conductive substrates, and the signal of Pt arises from the conductive coating of Pt on the sample surface by sputtering [37]. The EDS elemental mapping of composites also provides an even element distribution of Ti, Co and S (Figure S3).

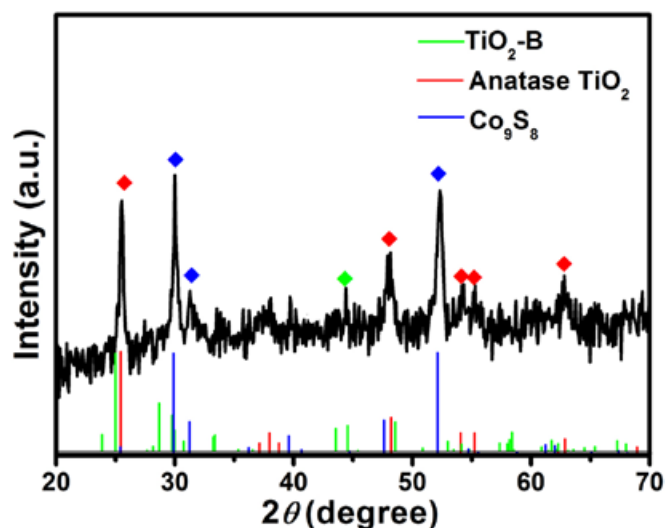


Figure 2. XRD pattern of the TiO₂ nanobelt@Co₉S₈ composites.

The morphology of TiO₂ nanobelt@Co₉S₈ composites was characterized by SEM and TEM techniques (Figure 3). The SEM image in Figure 3a clearly shows that some nanoparticles are evenly anchored on TiO₂ nanobelts, implying the formation of TiO₂ nanobelt@Co₉S₈ composites. Figure 3b exhibits its low magnified TEM images. It can be clearly observed that the TiO₂ nanobelt is uniformly coated with some small nanoparticles, which agrees well with the SEM data. The high magnified TEM image in Figure 3c shows the clear morphology of single TiO₂ nanobelt@Co₉S₈ composite. As can be seen, TiO₂ nanobelt presents an irregular porous nanostructure after acidizing and annealing. The related HRTEM image is demonstrated in Figure 3d, the d-spacings at 0.299 and 0.34 nm agree well with those from (311) planes of Co₉S₈ and (101) planes of TiO₂. The overlap of lattice fringes shows that small Co₉S₈ nanoparticles are grown on the surface of TiO₂ nanobelt likely induced by some chemical force effect. The SEM and TEM images of TiO₂ nanobelts and Co₉S₈ nanoparticles are also given as control samples (Figure S4). The nitrogen adsorption-desorption measurement was carried out to determine the surface area of TiO₂ nanobelt@Co₉S₈ composites. As shown in Figure S5a, a type-IV isotherm with a distinct hysteric loop for P/P_0 ranges from 0.5 to 1.0 could be observed, suggesting the mesoporous structure in the product. The surface area of TiO₂ nanobelt@Co₉S₈ composites is estimated as ~32.2 m²·g⁻¹. The pore size ranges from 23 to 38 nm and the main peak is located at 38 nm (Figure S5b), which is in agreement with what observed in TEM images. As seen in the previous paper, the low surface area can suppress the unnecessary side reaction, such as inevitable electrolyte decomposition and formation of solid electrolyte interface (SEI) [38,39]. Thus, it could be supposed that the hierarchical mesoporous TiO₂ nanobelt@Co₉S₈ composites as anode materials should present good lithium storage performance.

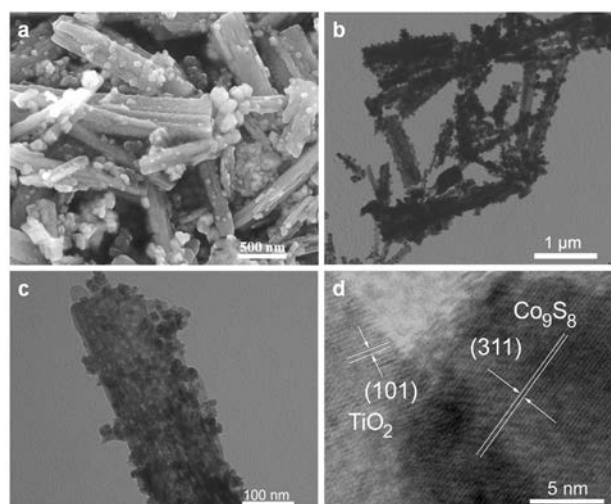


Figure 3. SEM image (a), TEM images (b,c) and HRTEM image (d) of the TiO₂ nanobelt@Co₉S₈ composites.

3.2. Electrochemical Performance of TiO₂ Nanobelt@Co₉S₈ Composites for LIBs

The electrochemical performances of TiO₂ nanobelt@Co₉S₈ composites for LIBs were tested (Figure 4). Figure 4a shows the cyclic voltammetry (CV) curves in a voltage window of 0.01–3.0 V at a scan rate of 0.1 mV·s⁻¹. In the first cathodic scan, the strong cathodic peak located at 1.13 V is likely to come from the reduction of Co₉S₈ to metallic Co, which is ascribed to the conversion reaction: $\text{Co}_9\text{S}_8 + 16\text{Li}^+ \rightarrow 9\text{Co} + 8\text{Li}_2\text{S}$ [40]. A small wide peak located at ~1.70 V is attributed to the formation of anatase Li_xTiO₂, corresponding to reaction equations: $x\text{Li}^+ + xe^- + \text{TiO}_2 \rightarrow \text{Li}_x\text{TiO}_2$ [31]. The wide peak at 0.76 V is related to the electrolyte decomposition and formation of SEI layer [38,39]. Inversely, a sharp anodic peak around 2.02 V can be assigned to the reversible oxidation of metallic Co, which overlaps with the charge process of Li⁺ deintercalation from the anatase framework (Li_xTiO₂) [31]. Another two pairs of peaks located at 1.48/1.57 V and 1.54/1.65 V are ascribed to the surfaced-confined charge-transfer process (faradic pseudocapacitive lithium storage behavior) of TiO₂-B [31]. The CV curves of TiO₂ nanobelt further confirm the coexistence of anatase TiO₂ and TiO₂-B (Figure S6a). Figure 4b shows the galvanostatic discharge/charge voltage profiles of TiO₂ nanobelt@Co₉S₈ composites for the first, second and fifth cycles over 0.01–3.0 V at 0.1 A·g⁻¹. The first discharge curve shows multiple voltage plateaus mainly located at 1.6 and 1.2 V, which is in agreement with the redox peaks observed from CV results. The initial reversible capacity and coulombic efficiency of TiO₂ nanobelt@Co₉S₈ composites could reach 714 mAh·g⁻¹ and 74%, respectively. The irreversible capacity for the first cycle could result from the electrolyte decomposition and formation of SEI layer, which is very similar to that of transition metal oxides-based anodes [41,42]. Besides, it also arises from the solvated lithium intercalation and subsequent reduction of the solvent [43]. The irreversible capacities are largely dependent on the external surface area of the electrode and also plausibly related to the irreversible conversion reaction of Co₉S₈ for the first cycle and volume change of the electrode during the conversion process [44]. The cycling performance of TiO₂ nanobelt@Co₉S₈ composites shows that a high reversible capacity of 889 mAh·g⁻¹ can be achieved after 100 cycles (Figure 4c), which is far higher than that of single TiO₂ nanobelt (Figure S6b). The capacity increase upon cycling is mainly from the pseudocapacitive lithium storage of TiO₂ nanobelt and Co₉S₈ nanoparticles [8]. Such good electrochemical performance could be attributed to the designed hierarchical composites. The Co₉S₈ nanoparticles attached to TiO₂ nanobelt can provide high capacity and improve conductivity for overall composites. Their small particle size and uniform dispersion of Co₉S₈ can effectively inhibit volume changes during cycling. Moreover, 1D TiO₂ nanobelt can enhance the electron transfer efficiency, and the TiO₂-B in the TiO₂ nanobelt will lead to a higher reversible capacity compared to pure anatase TiO₂ [45]. The interfaces between anatase and TiO₂-B nanodomains can also contribute to

additional lithium storage capacity [31]. More importantly, the anatase/TiO₂-B nanobelt as backbone for Co₉S₈ can suppress the separation of Co₉S₈, its inherent cycling stability of TiO₂ can also hinder the capacity loss of Co₉S₈ upon cycling. All the above factors facilitate the good electrochemical performances of TiO₂ nanobelt@Co₉S₈ composites. The rate capability is another important kinetic factor to evaluate the electrochemical performance of TiO₂ nanobelt@Co₉S₈ composites. As presented in Figure 4d, the average reversible capacity of TiO₂ nanobelt@Co₉S₈ composites at a current density of 0.1, 0.2, 0.5, 1, 2 and 5 A·g⁻¹ is 707, 676, 605, 502, 473 and 260 mAh·g⁻¹, respectively, which is superior to those of the TiO₂ nanobelt. The electrochemical performances of TiO₂ nanobelt@Co₉S₈ composites at large current densities such as 1, 2 and 5 A·g⁻¹ are superior to those of Co₉S₈ nanoparticles. Surprisingly, when the current density returns back to 0.1 A·g⁻¹, the reversible capacity is still as high as 776 mAh·g⁻¹, which is higher than initial capacity value. This phenomenon is likely attributed to the enhanced capacitance contribution resulting from the so-called electrochemical milling effect. All the results mentioned show that the TiO₂ nanobelt@Co₉S₈ composites could be considered as potential anode materials to be applied for LIBs.

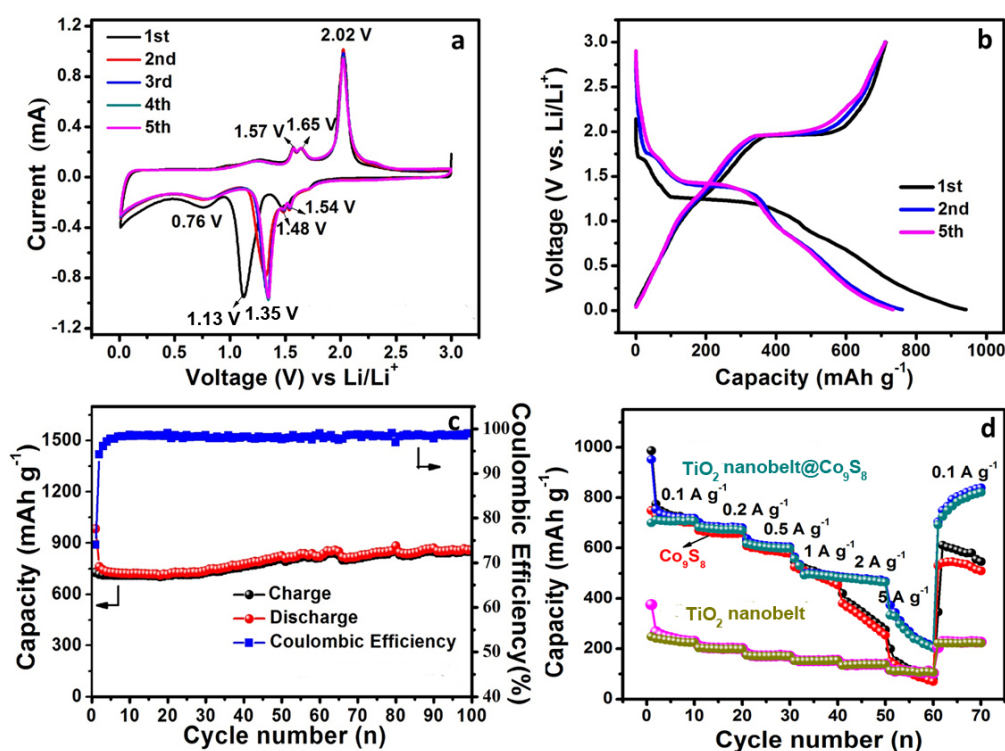


Figure 4. Cyclic voltammograms (a), galvanostatic discharge/charge profiles (b), cycling performances (c) of the TiO₂ nanobelt@Co₉S₈ composites and (d) rate performances of the TiO₂ nanobelt@Co₉S₈ composites, TiO₂ nanobelts and Co₉S₈ nanoparticles.

Figure 5a presents the cycling performances of TiO₂ nanobelt@Co₉S₈ composites, TiO₂ nanobelts and Co₉S₈ nanoparticles at 1 A·g⁻¹. Although the cycling stability of TiO₂ nanobelt is the best among three kinds of materials, its reversible capacity is only 216 mAh·g⁻¹. The reversible capacity of TiO₂ nanobelt@Co₉S₈ composites could retain at 369 mAh·g⁻¹ after 100 cycles. The electrochemical impedance spectra (EIS) were tested to further investigate the electrode process kinetics of three kinds of electrodes (Figure 5b). For all the electrodes before cycling, the depressed semicircle at high-to-medium frequencies is attributed to charge-transfer impedance (R_{ct}), and a slope at low frequencies is associated with ion diffusion process inside the electrode (constant phase element, CPE) [46]. After cycling, the depressed semicircles are related to two overlapped interface impedances (SEI and R_{ct}) [35]. The phase angle of slope for TiO₂ is close to 45°, suggesting a diffusion-controlled feature of lithium

insertion/extraction. The phase angles of slope for both TiO_2 nanobelt@ Co_9S_8 composites and Co_9S_8 are greater than 45° , indicating significant capacitive component in lithium insertion/extraction [8]. Compared to the fresh electrodes, the decrease of R_{ct} for all the cycled electrodes suggests the electrochemically activation of anodes [47]. The relatively small R_s , SEI and R_{ct} verify effective lithium and electron transfer of this composite during cycling.

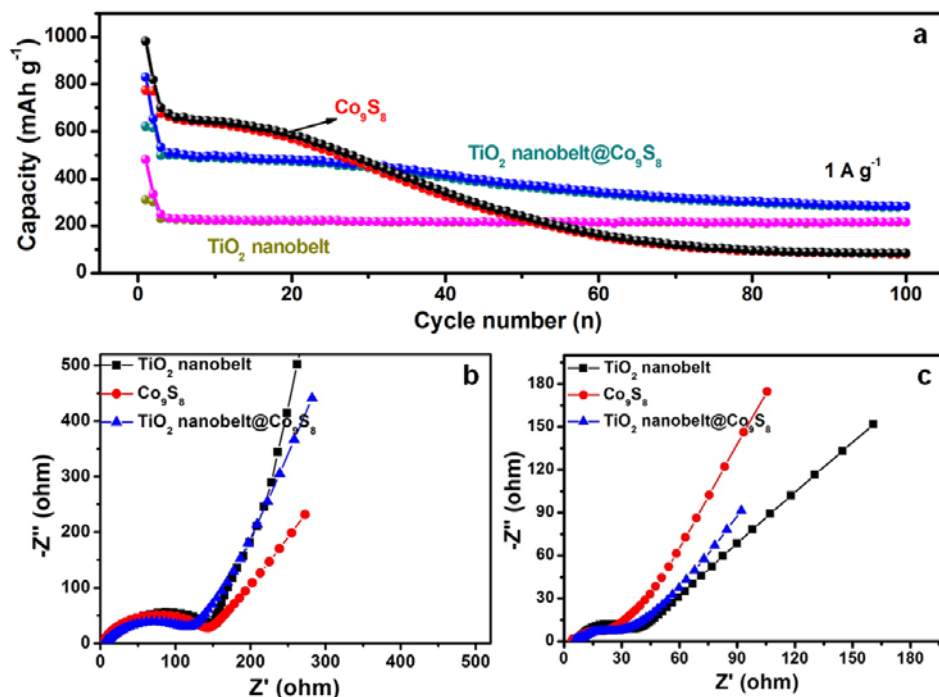


Figure 5. Cycling performances (a), electrochemical impedance spectra (EIS) of TiO_2 nanobelts, Co_9S_8 nanoparticles and TiO_2 nanobelt@ Co_9S_8 composites: before cycling (b), and after cycling (c).

3.3. Electrochemical Performance of TiO_2 Nanobelt@ Co_9S_8 Composites for SIBs

The electrochemical performances of TiO_2 nanobelt@ Co_9S_8 composites, TiO_2 nanobelt and Co_9S_8 nanoparticles for SIBs were also investigated (Figure 6). The CV curves are shown in Figure 6a, in the first cathodic scan, a strong peak located at ~ 0.46 V is likely to come from the formation of SEI film, and a small peak at 0.25 V is attributed to the intercalation process of Na^+ into the TiO_2 lattice [28]. The wide peaks located at ~ 1.13 V and 0.86 V are commonly attributed to the formation of $\text{Na}_x\text{Co}_9\text{S}_8$ and further reduction process to Co and Na_2S , respectively. The cathodic peak for the second cycle shifts to ~ 0.89 V, owing to irreversible structural rearrangement of Co_9S_8 . For the anodic process, an intense oxidation peak at ~ 1.76 V could be assigned to the oxidation reaction of Co metal to form Co_9S_8 or $\text{Na}_x\text{Co}_9\text{S}_8$ due to the irreversible reaction [48], which is in good accordance with previous reports [49]. The wide peak at ~ 0.52 V is associated with oxidation process of Na_xTiO_2 to TiO_2 and $\text{Na}_{1-x}\text{TiO}_2$ [50]. The overlap of all the cathodic and anodic peaks in subsequent cycles demonstrates the good reversibility of TiO_2 nanobelt@ Co_9S_8 composites. Moreover, two sloping voltage plateau located at about 0.9 and 0.5 V appear in the first discharge curves, while for the following cycles, only one obvious discharge voltage plateau can be found, which is located at around 0.9 V. For all of the charge process, just a wide voltage plateau is observed. The wide voltage plateau indicate the overlap of electrochemical reaction of TiO_2 and Co_9S_8 electrodes. All of the voltage plateaus in the discharge/charge curves of TiO_2 nanobelt@ Co_9S_8 composites can agree with the corresponding CV curves (Figure 6b).

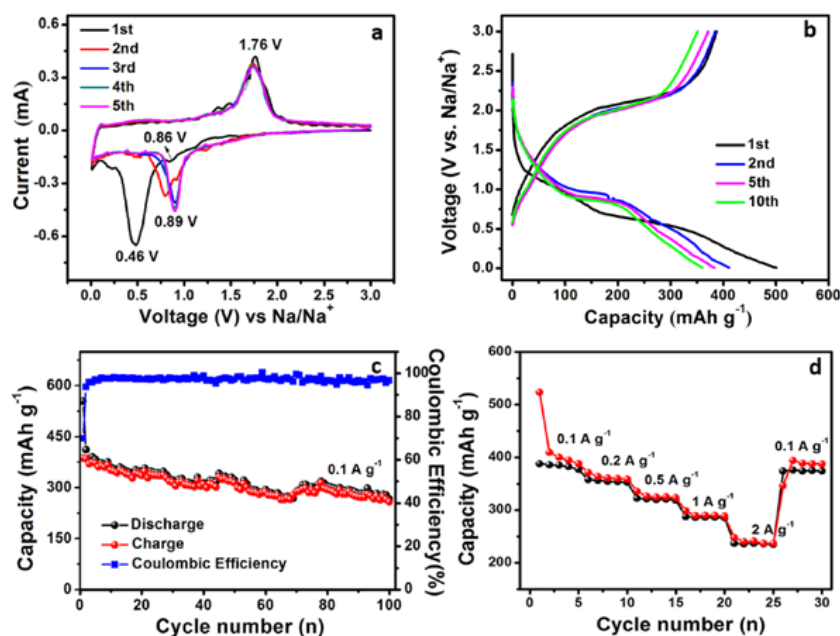


Figure 6. Cyclic voltammograms (a), galvanostatic discharge/charge profiles (b), cycling performances (c,d) rate performances of the TiO_2 nanobelt@ Co_9S_8 composites for SIBs.

Figure 6c shows the cycling performance of TiO_2 nanobelt@ Co_9S_8 composites at $0.1 \text{ A}\cdot\text{g}^{-1}$. The initial discharge and charge capacity can reach 554 and $387 \text{ mAh}\cdot\text{g}^{-1}$, respectively. After 100 cycles, the reversible capacity can still maintain at $258 \text{ mAh}\cdot\text{g}^{-1}$, displaying good cycling stability of TiO_2 nanobelt@ Co_9S_8 composites. The rate capability of TiO_2 nanobelt@ Co_9S_8 composites are shown in Figure 6d. The reversible capacity is 388 , 358 , 322 , 288 and $237 \text{ mAh}\cdot\text{g}^{-1}$ at 0.1 , 0.2 , 0.5 , 1 and $2 \text{ A}\cdot\text{g}^{-1}$, respectively. When the current density goes back to $0.1 \text{ A}\cdot\text{g}^{-1}$, the reversible capacity can return to $374 \text{ mAh}\cdot\text{g}^{-1}$. The cycling performance and rate capacity of TiO_2 nanobelt@ Co_9S_8 composites are better than those of single TiO_2 and Co_9S_8 for SIBs (Figure S7).

The EIS of three kinds of electrodes for SIBs were also measured (Figure S8), compared to fresh electrodes, all of the cycled electrodes exhibit smaller R_{ct} , and the R_{ct} of TiO_2 @ Co_9S_8 is located between TiO_2 and Co_9S_8 , which is possibly resulted from the good conductivity of Co_9S_8 . The phase angles of slope for these electrodes are similar to those of LIBs. The TiO_2 nanobelt@ Co_9S_8 composites with good electrochemical performances are of great potential to be used for both LIBs and SIBs.

4. Conclusions

In summary, we have successfully synthesized mixed phase TiO_2 nanobelt@ Co_9S_8 composites. As new anode materials, they show high specific capacities and good cycling performances for both LIBs and SIBs. After 100 cycles, their reversible capacity for LIBs can retain at 889 and $369 \text{ mAh}\cdot\text{g}^{-1}$ at 0.1 and $1 \text{ A}\cdot\text{g}^{-1}$, respectively. Besides, an initial reversible capacity of $387 \text{ mAh}\cdot\text{g}^{-1}$ can be obtained at $0.1 \text{ A}\cdot\text{g}^{-1}$ for SIBs. Such good electrochemical performances of TiO_2 nanobelt@ Co_9S_8 composites could be attributed to the hierarchical nanostructure and synergistic effect of Co_9S_8 nanoparticles and anatase/ TiO_2 -B nanobelts.

Supplementary Materials: The following are available online at <http://www.mdpi.com/2079-4991/7/9/252/s1>, Figure S1: XRD patterns and Raman spectra of (a) and (c) as-prepared TiO_2 nanobelts and (b) and (d) TiO_2 nanobelts obtained by a heat treatment of $650 \text{ }^\circ\text{C}$ under Ar/H_2 atmosphere, respectively, Figure S2: EDS spectrum of the as-prepared TiO_2 nanobelt@ Co_9S_8 composites (the inset is the molar ratio of element Ti, Co and S, respectively), Figure S3: SEM image corresponding to EDS elemental mapping of Ti, Co and S of as-prepared TiO_2 nanobelt@ Co_9S_8 composites, Figure S4: SEM images (a) and (c), TEM images (b) and (d) of TiO_2 nanobelts and Co_9S_8 nanoparticles, respectively, Figure S5: Nitrogen adsorption-desorption isotherm (a) and pore size distribution (b) of TiO_2 nanobelt@ Co_9S_8 composites at 77.3 K , Figure S6: CV curves (a) of TiO_2

nanobelts for the first five cycles at a scan rate of $0.1 \text{ mV}\cdot\text{s}^{-1}$ and cycling performances (b) of TiO_2 nanobelts at $0.1 \text{ A}\cdot\text{g}^{-1}$, Figure S7: Cycling performances (a) and (b) at $0.1 \text{ A}\cdot\text{g}^{-1}$, rate capacities (c) and (d) at different current densities of TiO_2 nanobelts and Co_9S_8 nanoparticles for SIBs, Figure S8: Electrochemical impedance spectra (EIS) of (a) before cycling and (b) after cycling 30 cycles of TiO_2 nanobelts, Co_9S_8 nanoparticles and TiO_2 nanobelt@ Co_9S_8 composites.

Acknowledgments: This work was supported by the National Nature Science Foundations of China (No. 51502160, 51272223 and 51772257), Natural Science Foundation of Shandong Province (No. ZR2015EQ001), and Applied Basic Research Foundation of Qingdao City (No. 16-5-1-93-jch)

Author Contributions: Yanli Zhou and Jian Tian conceived and designed the experiments; Qian Zhu performed the experiments; all authors analyzed the data; Yanli Zhou, Jian Tian and Fuyi Jiang wrote the paper; all authors discussed the results and commented on the paper.

Conflicts of Interest: The authors declare no conflicts of interest.

References

1. Tarascon, J.M.; Armand, M. Issues and challenges facing rechargeable lithium batteries. *Nature* **2001**, *414*, 359–367. [[CrossRef](#)] [[PubMed](#)]
2. Gao, X.P.; Yang, H.X. Multi-electron reaction materials for high energy density batteries. *Energy Environ. Sci.* **2010**, *3*, 174–189. [[CrossRef](#)]
3. Yan, Z.; Liu, L.; Shu, H.; Yang, X.; Wang, H.; Tan, J.; Zhou, Q.; Huang, Z.; Wang, X. A tightly integrated sodium titanate-carbon composite as an anode material for rechargeable sodium ion batteries. *J. Power Sources* **2015**, *274*, 8–14. [[CrossRef](#)]
4. Liang, M.; Zhi, L. Graphene-based electrode materials for rechargeable lithium batteries. *J. Mater. Chem.* **2009**, *19*, 5871–5878. [[CrossRef](#)]
5. Zhou, Y.; Jiang, X.; Chen, L.; Yue, J.; Xu, H.; Yang, J.; Qian, Y. Novel mesoporous silicon nanorod as an anode material for lithium ion batteries. *Electrochim. Acta* **2014**, *127*, 252–258. [[CrossRef](#)]
6. Xu, Y.; Zhu, Y.; Liu, Y.; Wang, C. Electrochemical performance of porous carbon/tin composite anodes for sodium-ion and lithium-ion batteries. *Adv. Energy Mater.* **2013**, *3*, 128–133. [[CrossRef](#)]
7. Zhu, C.; Mu, X.; Aken, P.A.; Yu, Y.; Maier, J. Single-layered ultrasmall nanoplates of MoS_2 embedded in carbon nanofibers with excellent electrochemical performance for lithium and sodium storage. *Angew. Chem. Int. Ed.* **2014**, *53*, 2152–2156. [[CrossRef](#)] [[PubMed](#)]
8. Zhou, Y.; Yan, D.; Xu, H.; Feng, J.; Jiang, X.; Yue, J.; Yang, J.; Qian, Y. Hollow nanospheres of mesoporous Co_9S_8 as a high-capacity and long-life anode for advanced lithium ion batteries. *Nano Energy* **2015**, *12*, 528–537. [[CrossRef](#)]
9. Zhang, X.; Ji, G.; Liu, W.; Quan, B.; Liang, X.; Shang, C.; Cheng, Y.; Du, Y. Thermal conversion of an Fe_3O_4 @metal-organic framework: A new method for an efficient Fe-Co/nanoporous carbon microwave absorbing material. *Nanoscale* **2015**, *7*, 12932–12942. [[CrossRef](#)] [[PubMed](#)]
10. Ma, Q.; Wang, W.; Zeng, P.; Fang, Z. Effects of binders on electrochemical properties of the SnS_2 nanostructured anode of the lithium-ion batteries. *Langmuir* **2017**, *33*, 2141–2147. [[CrossRef](#)] [[PubMed](#)]
11. Wu, Q.L.; Li, J.; Deshpande, R.D.; Subramanian, N.; Rankin, S.E.; Yang, F.; Cheng, Y.T. Aligned TiO_2 nanotube arrays as durable lithium-ion battery negative electrodes. *J. Phys. Chem. C* **2012**, *116*, 18669–18677. [[CrossRef](#)]
12. Han, H.; Song, T.; Lee, E.K.; Devadoss, A.; Jeon, Y.; Ha, J.; Chung, Y.C.; Choi, Y.M.; Jung, Y.G.; Paik, U. Dominant factors governing the rate capability of a TiO_2 nanotube anode for high power lithium ion batteries. *ACS Nano* **2012**, *6*, 8308–8315. [[CrossRef](#)] [[PubMed](#)]
13. Su, D.; Dou, S.; Wang, G. Anatase TiO_2 : Better anode material than amorphous and rutile phases of TiO_2 for Na-ion batteries. *Chem. Mater.* **2015**, *27*, 6022–6029. [[CrossRef](#)]
14. Bi, Z.; Paranthaman, M.P.; Menchhofer, P.A.; Dehoff, R.R.; Bridges, C.A.; Chi, M.; Guo, B.; Sun, X.G.; Dai, S. Self-organized amorphous TiO_2 nanotube arrays on porous Ti foam for rechargeable lithium and sodium ion batteries. *J. Power Sources* **2013**, *222*, 461–466. [[CrossRef](#)]
15. Qiu, J.; Li, S.; Gray, E.; Liu, H.; Gu, Q.F.; Sun, C.; Lai, C.; Zhao, H.; Zhang, S. Hydrogenation synthesis of blue TiO_2 for high-performance lithium-ion batteries. *J. Phys. Chem. C* **2014**, *118*, 8824–8830. [[CrossRef](#)]
16. Li, J.M.; Wan, W.; Zhou, H.H.; Li, J.J.; Xu, D.S. Hydrothermal synthesis of TiO_2 (B) nanowires with ultrahigh surface area and their fast charging and discharging properties in Li-ion batteries. *Chem. Commun.* **2011**, *47*, 3439–3441. [[CrossRef](#)] [[PubMed](#)]

17. Brutti, S.; Gentili, V.; Menard, H.; Scrosati, B.; Bruce, P.G. TiO₂-(B) nanotubes as anodes for lithium batteries: Origin and mitigation of irreversible capacity. *Adv. Energy Mater.* **2012**, *2*, 322–327. [[CrossRef](#)]
18. Seisenbaeva, G.A.; Nedelec, J.M.; Daniel, G.; Tiseanu, C.; Parvulescu, V.; Pol, V.G.; Abrego, L.; Kessler, V.G. Mesoporous anatase TiO₂ nanorods as thermally robust anode materials for Li-ion batteries: Detailed insight into the formation mechanism. *Chem. Eur. J.* **2013**, *19*, 17439–17444. [[CrossRef](#)] [[PubMed](#)]
19. Shim, H.W.; Lee, D.K.; Cho, I.S.; Hong, K.S.; Kim, D.W. Facile hydrothermal synthesis of porous TiO₂ nanowire electrodes with high-rate capability for Li ion batteries. *Nanotechnology* **2010**, *21*, 255706. [[CrossRef](#)] [[PubMed](#)]
20. Wang, H.; Guan, C.; Wang, X.; Fan, H.J. A high energy and power Li-ion capacitor based on a TiO₂ nanobelt array anode and a graphene hydrogel cathode. *Small* **2015**, *11*, 1470–1477. [[CrossRef](#)] [[PubMed](#)]
21. Wen, W.; Wu, J.; Jiang, Y.; Yu, S.; Bai, J.; Cao, M.; Cui, J. Anatase TiO₂ ultrathin nanobelts derived from room-temperature-synthesized titanates for fast and safe lithium storage. *Sci. Rep.* **2015**, *5*, 11804. [[CrossRef](#)] [[PubMed](#)]
22. Tian, J.; Zhao, Z.; Kumar, A.; Boughton, R.I.; Liu, H. Recent progress in design, synthesis, and applications of one-dimensional TiO₂ nanostructured surface heterostructures: A review. *Chem. Soc. Rev.* **2014**, *43*, 6920–6937. [[CrossRef](#)] [[PubMed](#)]
23. Yu, L.; Wang, Z.; Zhang, L.; Wu, H.B.; Lou, X.W. TiO₂ nanotube arrays grafted with Fe₂O₃ hollow nanorods as integrated electrodes for lithium-ion batteries. *J. Mater. Chem. A* **2013**, *1*, 122–127. [[CrossRef](#)]
24. Mao, M.; Mei, L.; Guo, D.; Wu, L.; Zhang, D.; Li, Q.; Wang, T. High electrochemical performance based on the TiO₂ nanobelt@few-layered MoS₂ structure for lithium-ion batteries. *Nanoscale* **2014**, *6*, 12350–12353. [[CrossRef](#)] [[PubMed](#)]
25. Huang, H.; Fang, J.; Xia, Y.; Tao, X.; Gan, Y.; Du, J.; Zhu, W.; Zhang, W. Construction of sheet-belt hybrid nanostructures from one-dimensional mesoporous TiO₂ (B) nanobelts and graphene sheets for advanced lithium-ion batteries. *J. Mater. Chem. A* **2013**, *1*, 2495–2500. [[CrossRef](#)]
26. Huang, P.; Yuan, D.D.; Zhang, H.Z.; Cao, Y.L.; Li, G.R.; Yang, H.X.; Gao, X.P. Electrochemical sodium storage of TiO₂ (B) nanotubes for sodium ion batteries. *RSC Adv.* **2013**, *3*, 12593–12597. [[CrossRef](#)]
27. Wu, L.; Bresser, D.; Buchholz, D.; Passerini, S. Nanocrystalline TiO₂ (B) as anode material for sodium-ion batteries. *J. Electrochem. Soc.* **2015**, *162*, A3052–A3058. [[CrossRef](#)]
28. Yan, Z.; Liu, L.; Tan, J.; Zhou, Q.; Huang, Z.; Xia, D.; Shu, H.; Yang, X.; Wang, X. One-pot synthesis of bicrystalline titanium dioxide spheres with a core-shell structure as anode materials for lithium and sodium ion batteries. *J. Power Sources* **2014**, *269*, 37–45. [[CrossRef](#)]
29. Zúkalová, M.; Kalbac, M.; Kavan, L.; Exnar, I.; Graetzel, M. Pseudocapacitive lithium storage in TiO₂ (B). *Chem. Mater.* **2005**, *17*, 1248–1255. [[CrossRef](#)]
30. Liu, H.; Bi, Z.; Sun, X.G.; Unocic, R.R.; Paranthaman, M.P.; Dai, S.; Brown, G.M. Mesoporous TiO₂-B microspheres with superior rate performance for lithium ion batteries. *Adv. Mater.* **2011**, *23*, 3450–3454. [[CrossRef](#)] [[PubMed](#)]
31. Wu, Q.; Xu, J.; Yang, X.; Lu, F.; He, S.; Yang, J.; Fan, H.J.; Wu, M. Ultrathin anatase TiO₂ nanosheets embedded with TiO₂-B nanodomains for lithium-ion storage: Capacity enhancement by phase boundaries. *Adv. Energy Mater.* **2015**, *5*, 1–9. [[CrossRef](#)]
32. Xia, H.; Xiong, W.; Lim, C.K.; Yao, Q.; Wang, Y.; Xie, J. Hierarchical TiO₂-B nanowire@ α -Fe₂O₃ nanothorn core-branch arrays as superior electrodes for lithium-ion microbatteries. *Nano Res.* **2014**, *7*, 1797–1808. [[CrossRef](#)]
33. Zhang, J.; Shen, J.; Wang, T.; Zhang, H.; Wei, C.; Zhang, K.; Yue, Y. TiO₂-B nanoribbons anchored with NiO nanosheets as hybrid anode materials for rechargeable Lithium Ion Batteries. *CrystEngComm* **2015**, *17*, 1710–1715. [[CrossRef](#)]
34. Tian, J.; Sang, Y.; Zhao, Z.; Zhou, W.; Wang, D.; Kang, X.; Liu, H.; Wang, J.; Chen, S.; Cai, H.; Huang, H. Enhanced photocatalytic performances of CeO₂/TiO₂ nanobelt heterostructures. *Small* **2013**, *9*, 3864–3872. [[CrossRef](#)] [[PubMed](#)]
35. Zhou, Y.; Yan, D.; Xu, H.; Liu, S.; Yang, J.; Qian, Y. Multiwalled carbon nanotube@a-C@Co₉S₈ nanocomposites: A high-capacity and long-life anode material for advanced lithium ion batteries. *Nanoscale* **2015**, *7*, 3520–3525. [[CrossRef](#)] [[PubMed](#)]

36. Prochazka, J.; Kavan, L.; Zukalova, M.; Frank, O.; Kalbac, M.; Zukal, A.; Klementova, M.; Carbone, D.; Graetzel, M. Novel synthesis of the TiO₂ (B) multilayer templated films. *Chem. Mater.* **2009**, *21*, 1457–1464. [[CrossRef](#)]
37. Chen, C.; Hu, X.; Jiang, Y.; Yang, Z.; Hu, P.; Huang, Y. TiO₂-B Nanosheets/ Anatase Nanocrystals Co-Anchored on Nanoporous Graphene: In Situ Reduction-Hydrolysis Synthesis and Their Superior Rate Performance as an Anode Material. *Chem. Eur. J.* **2014**, *20*, 1383–1388. [[CrossRef](#)] [[PubMed](#)]
38. Wang, Y.; Wu, J.; Tang, Y.; Lu, X.; Yang, C.; Qin, M.; Huang, F.; Li, X.; Zhang, X. Phase-controlled synthesis of cobalt sulfides for lithium ion batteries. *ACS Appl. Mater. Interfaces* **2012**, *4*, 4246–4250. [[CrossRef](#)] [[PubMed](#)]
39. Nam, K.T.; Kim, D.W.; Yoo, P.J.; Chiang, C.Y.; Meethong, N.; Hammond, P.T.; Chiang, Y.M.; Belcher, A.M. Virus-enabled synthesis and assembly of nanowires for lithium ion battery electrodes. *Science* **2006**, *312*, 885–888. [[CrossRef](#)] [[PubMed](#)]
40. Shi, W.; Zhu, J.; Rui, X.; Cao, X.; Chen, C.; Zhang, H.; Hng, H.H.; Yan, Q. Controlled synthesis of carbon-coated cobalt sulfide nanostructures in oil phase with enhanced Li storage performances. *ACS Appl. Mater. Interfaces* **2012**, *4*, 2999–3006. [[CrossRef](#)] [[PubMed](#)]
41. Agubra, V.A.; Zuniga, L.; Flores, D.; Campos, H.; Villarreal, J.; Alcoutlabi, M. A comparative study on the performance of binary SnO₂/NiO/C and Sn/C composite nanofibers as alternative anode materials for lithium ion batteries. *Electrochim. Acta* **2017**, *224*, 608–621. [[CrossRef](#)]
42. Agubra, V.A.; Zuniga, L.; Garza, D.D.; Gallegos, L.; Pokhrel, M.; Alcoutlabi, M. Forcespinning: A new method for the mass production of Sn/C composite nanofiber anodes for lithium ion batteries. *Solid State Ion.* **2016**, *286*, 72–82. [[CrossRef](#)]
43. Yu, P.; Ritter, J.A.; White, R.E.; Popov, B.N. Ni-composite microencapsulated graphite as the negative electrode in lithium-ion batteries I. Initial irreversible capacity study. *J. Electrochem. Soc.* **2000**, *147*, 1280–1285. [[CrossRef](#)]
44. Liu, S.; Wang, J.; Wang, J.; Zhang, F.; Wang, L. Highly uniform Co₉S₈ nanoparticles grown on graphene nanosheets as advanced anode materials for improved Li-storage performance. *Appl. Surf. Sci.* **2016**, *390*, 86–91. [[CrossRef](#)]
45. Ren, Y.; Liu, Z.; Pourpoint, F.; Armstrong, A.R.; Grey, C.P.; Bruce, P.G. Nanoparticulate TiO₂ (B): An anode for lithium-ion batteries. *Angew. Chem.* **2012**, *124*, 2206–2209. [[CrossRef](#)]
46. Zuniga, L.; Agubra, V.; Flores, D.; Campos, H.; Villarreal, J.; Alcoutlabi, M. Multichannel hollow structure for improved electrochemical performance of TiO₂/Carbon composite nanofibers as anodes for lithium ion batteries. *J. Alloys Compd.* **2016**, *686*, 733–743. [[CrossRef](#)]
47. Amaresh, S.; Karthikeyan, K.; Jang, I.C.; Lee, Y.S. Single-step microwave mediated synthesis of CoS₂ anode material for high rate hybrid supercapacitors. *J. Mater. Chem. A* **2014**, *2*, 11099–11106. [[CrossRef](#)]
48. Liu, X.; Liu, H.; Zhao, Y.; Dong, Y.; Fan, Q.; Kuang, Q. Synthesis of the carbon-coated nanoparticle Co₉S₈ and its electrochemical performance as an anode material for sodium-ion batteries. *Langmuir* **2016**, *32*, 12593–12602. [[CrossRef](#)] [[PubMed](#)]
49. Han, F.; Tan, C.Y.J.; Gao, Z. Template-free formation of carbon nanotube-supported cobalt sulfide@carbon hollow nanoparticles for stable and fast sodium ion storage. *J. Power Sources* **2017**, *339*, 41–50. [[CrossRef](#)]
50. Yang, H.; Duh, J.G. Aqueous sol-gel synthesized anatase TiO₂ nanoplates with high-rate capabilities for lithium ion and sodium-ion batteries. *RSC Adv.* **2016**, *6*, 37160–37166. [[CrossRef](#)]

